Journal of Solid State Chemistry 183 (2010) 310–321

Contents lists available at ScienceDirect

Journal of Solid State Chemistry

journal homepage: www.elsevier.com/locate/jssc

Ionothermal syntheses of three transition-metal-containing polyoxotungstate hybrids exhibiting the photocatalytic and electrocatalytic properties

Wei-Lin Chen, Bao-Wang Chen, Hua-Qiao Tan, Yang-Guang Li *, Yong-Hui Wang, En-Bo Wang *

Key Laboratory of Polyoxometalate Science of Ministry of Education, Department of Chemistry, Northeast Normal University, Ren Min Street No. 5268, Changchun, Jilin 130024, PR China

ARTICLE INFO

Article history:
Received 3 October 2009
Received in revised form
14 November 2009
Accepted 18 November 2009
Available online 24 November 2009

Keywords:
Polyoxometalates
Ionic liquids
Ionothermal synthesis
Photocatalytic properties
Electrocatalytic properties

ABSTRACT

Employing the ionothermal synthesis approach, three new transition-metal-containing polyoxotungstate hybrids: $[Dmim]_2Na_3[SiW_{11}O_{39}Fe(H_2O)]\cdot H_2O$ (Dmim=1,3-Dimethylimidazole) (**1**), $[Emim]_9Na_8[(SiW_9O_{34})_3\{Fe_3(\mu_2\text{-}OH)_2(\mu_3\text{-}O)\}_3(WO_4)]\cdot 0.5H_2O$(Emim=1-Ethyl-3-meth-ylimidazole) (**2**) and $[Dmim]2[HMim]Na_6[(AsW_9O_{33})_2\{Mn^{III}(H_2O)\}_3]\cdot 3H_2O$ (Dmim=1,3-Dimethylimidazole; Mim=1-Methylimidazole) (**3**) have been synthesized in 1-ethyl-3-methyl imidazolium bromide ([Emim]Br) ionic liquids (ILs). Compound **1** possesses a 3-D open framework constructed from the mono-iron^{III}-substituted α-Keggin-type anion and the organic cations [Dmim]+ through the hydrogen bond interactions. Compound **2** contains a $[\{Fe_3^{III}(\mu_2\text{-}OH)_2(\mu_3\text{-}O)\}_3(\mu_4\text{-}WO_4)]$ cluster surrounded by three $[SiW_9O_{34}]^{10-}$ ligands, eight sodium cations and nine dissociative $[Emim]^+$ cations around the polyoxoanion. The polyoxoanion of **3** consists of a high-valent trinuclear-manganese (III)-substituted sandwiching polyoxoanion based on the $[\alpha\text{-}AsW_9O_{33}]^{9-}$ units. All the compounds are characterized by elemental analyses, IR, UV–vis spectra, TG-DTA and XRD analyses. The XPS and EPR spectra of Mn^{III} in **3** were studied. The photocatalytic and electrocatalytic properties, as well as the stabilities of **1**–**3** were also investigated.

© 2009 Elsevier Inc. All rights reserved.

1. Introduction

It is still an arduous researching project to explore suitable methods for the syntheses of novel polyoxometalates (POMs) along with the fast developments of POMs chemistry [1–6]. Consequently, finding an excellent solvent for the reactions is urgent for all the chemists working in the POMs fields. Ionic liquids (ILs), as a solvent composed of only cations and anions, firstly seize our attentions ascribing to their specific properties, low melting point, high ionic conductivity, non-volatility, non-flammability, high polarity, zero vapor pressure and relatively low viscosity [7–9]. Therefore, they may be good substitutes for the traditional solvents (water, some organic solvents such as methanol, acetonitrile, acetone, and so on) to synthesize new POMs-based clusters. Recently, ionothermal synthesis, as an excellent synthetic method, has been applied in the synthesis fields of zeolites [9–10], metal coordination polymers [11], supramolecular complexes [12] and metal organic frameworks (MOFs) [13]. ILs as the solvents play important parts in the ionothermal syntheses, they may bring some new particular advantages into the synthesis systems, involving anion control [11], chiral induction effects [13], hydrogen-bond-directing effects [14] and structural templating agents [15].

On the basis of the above considerations, we attempt to employ ionothermal synthesis to obtain novel POMs. The main reasons are as follows: Firstly, if the cations of ILs replace the inorganic cations of POMs, the polyanions will be recombined in this process, which may result in the isolations of more novel POMs-based clusters. Secondly, in traditional hydrothermal or solvothermal synthesis, the reaction temperature is limited attributed to the danger of explosion under higher temperature. However, ionothermal synthesis may avoid the hidden trouble, ascribing to the non-flammability and zero vapor pressure of ILs [7,8]. Thirdly, the weak coordination ability of ILs may bring more comfortable reaction environments for the self-assembly of the polyoxoanions. Fourthly, their low volatility and high soluble ability are beneficial for the obtainments of crystal products. Fifthly, new supermolecule materials will be obtained if the cation parts of ILs are combined with the polyoxoanions, which may attract most interests in the solid lubricants, biocatalysis and electrocatalysis [16–18]. Sixthly, they possess the tunable acidity, which may offer alterable reaction environments with different pH values for the synthesis of the polyoxoanions.

* Corresponding authors. Fax: +86 431 85098787.
E-mail addresses: liyg658@nenu.edu.cn (Y.-G. Li), wangeb889@nenu.edu.cn (E.-B. Wang).

0022-4596/$ - see front matter © 2009 Elsevier Inc. All rights reserved.
doi:10.1016/j.jssc.2009.11.016

In our previous work, we had firstly reported two new POMs-based hybrids synthesized in the ILs at atmospheric pressure [19]. Here, we continue our work and successfully obtained three new transition-metal-containing polyoxotungstate hybrids with ionothermal synthesis: $[Dmim]_2Na_3[SiW_{11}O_{39}Fe(H_2O)]\cdot H_2O$ (**1**), $[Emim]_9Na_8[(SiW_9O_{34})_3\{Fe_3(\mu_2\text{-}OH)_2(\mu_3\text{-}O)\}_3(WO_4)]\cdot 0.5H_2O$ (**2**) and $[Dmim]_2[HMim]Na_6[(AsW_9O_{33})_2\{Mn(H_2O)\}_3]\cdot 3H_2O$ (**3**). The investigations indicate that the ionothermal synthesis is suitable for synthesizing different kinds of POMs. All the three compounds were well characterized. Furthermore, their photocatalytic and electrocatalytic properties have also been investigated.

2. Experimental

2.1. Materials

All chemicals were commercially purchased and used without further purification. The ionic liquid [Emim]Br was synthesized according to the literature method [20] (The detailed synthesis method is in the caption of Scheme S1). $K_8[\beta_2\text{-}SiW_{11}O_{39}]\cdot 14H_2O$ [21], $Na_{10}[\alpha\text{-}SiW_9O_{34}]\cdot 20H_2O$ [22] and $Na_9[AsW_9O_{33}]\cdot 19.5H_2O$ [23] were synthesized according to the literatures and characterized by IR spectroscopy and TG analyses.

2.2. Physical measurements

Elemental analyses W, Si, Na, Fe, As and Mn were performed by a Leaman inductively coupled plasma (ICP) spectrometer, C, H and N were performed on a Perkin–Elmer 2400 CHN elemental analyzer. IR spectra were recorded in the range of 400–4000 cm^{-1} on an Alpha Centaurt FT/IR Spectrophotometer with pressed KBr pellets. Diffuse reflectance UV–vis spectra ($BaSO_4$ pellet) were obtained with a Varian Cary 500 UV–vis NIR spectrometer. UV–vis absorption spectra were obtained using a 752 PC UV–vis spectrophotometer. TG-DTA analyses were carried out on a Perkin–Elmer TGA7 instrument in flowing N_2 with a heating rate of 10 °C min^{-1}. XRD studies were performed with a Rigaku D/max-IIB X-ray diffractometer at a scanning rate of 1° per minute using Cu$K\alpha$ radiation (λ=1.5418 Å). XPS analyses were performed on a VG ESCALABMKII spectrometer with an Mg$K\alpha$ (1253.6 eV) X-ray source. The vacuum inside the analysis chamber was maintained at 6.2×10^{-6} Pa during the analyses. The EPR spectra were recorded with a Bruker ER 200D spectrometer at room temperature. All the electrochemical measurements and data collections were carried out on a CHI 660 electrochemical workstation connected to a personal computer at room temperature (25–30 °C). The media for the electrochemical and electrocatalytic experiments are all $0.5\,M\cdot H_2SO_4/NaSO_4$ (pH=4.50) solutions. A pHS-25B type pH meter was used for pH measurement. Platinum wire was used as the counter electrode and an Ag/AgCl was used as the reference electrode. Thrice-distilled water was used throughout the experiments. The gel filtration chromatography analysis of **2** was carried out with a 1 mL mixture of 1 mM each of $[P_2W_{15}Mo_2VO_{62}]^{8-}$ and **2** in a $0.5\,M\cdot H_2SO_4/NaSO_4$ (pH=4.50) solution passing through a 40 cm × 1 cm^2 Sephadex G-50 fine column previously equilibrated in the same solution (The detailed method is in the figure caption of Figure S15). The color of the solid sample **2** is orange, while the color of 1 mM **2** in the solution is yellow ascribed to the low concentration of **2** in the experiment.

2.3. Photocatalysis experiments

The aqueous solution was prepared by addition of the sample (30 mg for **1**, or 88 mg of **2** or 52 mg of **3**) to a 50 mL $0.5\,M\cdot H_2SO_4/Na_2SO_4$ (pH=4.50) solution of RhB dye (2×10^{-5} M) and then magnetically stirred in the dark for 50 min. The solution was exposed to UV irradiation from a 125 W Hg lamp at a distance of 3–4 cm between the liquid surface and the lamp. The solution was still stirred with a magnetic stir bar during irradiation. In total, 3 mL of samples were taken out from the beaker at different time intervals. The solution was used for UV–vis absorption spectrum analysis.

2.4. Synthesis

2.4.1. $[Dmim]_2Na_3[SiW_{11}O_{39}Fe(H_2O)]\cdot H_2O$ (1)

A mixture of [Bmim]Br (7.64 g, 40 mmol), $K_8[\beta_2\text{-}SiW_{11}O_{39}]\cdot 14H_2O$ (0.81 g, 0.25 mmol), $Fe(NO_3)_3\cdot 9H_2O$ (0.20 g, 0.5 mmol) and $NaVO_3$ (1 mmol, 0.12 g) was heated to 80 °C and stirred for half an hour in air. The mixture was then transferred to a Teflon-lined autoclave (23 mL) and kept at 160 °C for four days. After the autoclave was slowly cooled to room temperature, it was maintained for one day without opening, and then black crystals were filtered off, washed with acetone and dried in a desiccator at room temperature (yield 90% based on W). There is no vanadium element in **1**. Elemental analysis for $C_{10}H_{22}FeN_4Na_3O_{41}SiW_{11}$ (**1**) calcd. C, 3.96; H, 0.73; Fe, 1.84; N, 1.85; Na, 2.28; Si, 0.93; W, 66.75 (%); found: C, 3.99; H, 0.70; Fe, 1.82; N, 1.88; Na, 2.31; Si, 0.95; W, 65.69 (%). FT/IR data (cm^{-1}): 3060(br), 1561(s), 1457(m), 1332(w), 1165(s), 1091(w), 955(w), 904(s), 786(s), 673(w), 522(m) (Figure S19).

2.4.2. $[Emim]_9Na_8[(SiW_9O_{34})_3\{Fe_3(\mu_2\text{-}OH)2(\mu_3\text{-}O)\}_3(WO_4)]\cdot 0.5H_2O$ (2)

A mixture of [Bmim]Br (9.55 g, 50 mmol), $Na_{10}[\alpha\text{-}SiW_9O_{34}]\cdot 20H_2O$ (1.41 g, 0.5 mmol), $Fe(NO_3)_3\cdot 9H_2O$ (0.80 g, 2 mmol) and $Ce(NO_3)_3\cdot 6H_2O$ (0.22 g, 0.5 mmol) was heated to 80 °C and stirred for half an hour in air. The mixture was then transferred to a Teflon-lined autoclave (23 mL) and kept at 150 °C for one week. After the autoclave was slowly cooled to room temperature, it was kept for two days without opening, and then orange crystals were filtered off, washed with acetone and dried in a desiccator at room temperature (yield 75% based on W). There is no cerium element in **2**. Elemental analysis for $C_{54}H_{106}Fe_9N_{18}Na_8O_{115.5}Si_3W_{28}$ (**2**) calcd. C, 7.39; H, 1.22; Fe, 5.73; N, 2.87; Na, 2.10; Si, 0.96; W, 58.67 (%); found: C, 7.42; H, 1.20; Fe, 5.76; N, 2.90; Na, 2.13; Si, 0.92; W, 58.61 (%). FT/IR data (cm^{-1}): 3420(br), 3148(w), 3091(sh), 1636(m), 1571(s), 1457(m), 1394(w), 1338(w), 1170(s), 1089(w), 991(w), 947(m), 903(s), 799(w), 733(sh), 648(w), 622(s), 520(m) (Figure S20).

2.4.3. $[Dmim]_2[HMim]Na_6[(AsW_9O_{33})_2\{Mn^{III}(H_2O)\}_3]\cdot 3H_2O$ (3)

A mixture of [Bmim]Br (5.73 g, 30 mmol), $Na_9[AsW_9O_{33}]\cdot 19.5H_2O$ (1.19 g, 0.15 mmol), $MnCl_2\cdot 4H_2O$ (0.15 g, 0.75 mmol) and $K_2S_2O_8$ (0.41 g, 1.5 mmol) was heated to 80 °C and stirred for half an hour in air, the color of the mixture changed from yellow to purple. The mixture was then transferred to a Teflon-lined autoclave (23 mL) and kept at 180 °C for six days. After the autoclave was slowly cooled to room temperature, it was kept for one day without opening, and then purple crystals were filtered off from the final purple mixture, washed with acetone and dried in a desiccator at room temperature (yield 55% based on W). Elemental analysis for $C_{14}H_{37}As_2Mn_3N_6Na_6O_{72}W_{18}$ (**3**) calcd. C, 3.23; H, 0.72; As, 2.88; Mn, 3.17; N, 1.62; Na, 2.65; W, 63.60 (%); found: C, 3.27; H, 0.69; As, 2.92; Mn, 3.13; N, 1.65; Na, 2.68; W, 63.54. FT/IR data (cm^{-1}): 3395(br), 3109(br), 1619(m), 1571(m), 1437(br), 1169(s), 1086(m), 952(s), 887(s), 729(sh), 621(w), 486(sh) (Figure S21).

2.5. X-ray crystallography

The crystallographic data of **1**–**3** were collected at 293(2) K on a Rigaku R-axis Rapid IP diffractometer using graphite monochromatic Mo$K\alpha$ radiation (λ=0.71073 Å). Numerical absorption corrections were applied. Data processing was accomplished with the RAXWISH processing program. A total of 25 577 reflections for **1** were collected, of which 6011 reflections were unique, a total of 67 155 reflections for **2** were collected, of which 31 226 reflections were unique, and also a total of 54 670 reflections for **3** were collected, of which 17 378 reflections were unique. The structures of **1**–**3** were solved by the direct method and refined by the full-matrix least-squares method on F^2 using the SHELXTL-97 crystallographic software package [24,25]. Crystal data and structure refinements for **1**–**3** are summarized in Table 1. Selected bond lengths and angles of **1**–**3** are given in Tables S1, S2 and S5, respectively.

3. Results and discussion

3.1. Synthesis discussion

The successful isolations of compounds **1–3** depend on the ionothermal synthesis strategy. So far, it is a very promising and versatile synthetic technique for assembling novel POMs-based clusters [26,27]. There are some main affecting factors in the ionothermal synthesis, such as the dosage of ILs, the molar ratio of the reactants and ILs, the pH value of the reaction systems, reaction time and temperature, crystallization time and so on.

During the synthesis of **1**–**3**, 1-ethyl-3-methyl imidazolium bromide [Emim]Br was used as the solvent, [Emim]Br was solid state at room temperature before the reactions, while it started to transfer to be liquid state and participated in the synthesis under the ionothermal conditions. After the reactions, it was liquid state finally. All the reactants dissolved in the ILs were excessive during

Table 1
Crystal data and structure refinements for **1–3**.

	1	2	3
Empirical formula	$C_{10}H_{22}FeN_4Na_3O_{41}SiW_{11}$	$C_{54}H_{106}Fe_9N_{18}Na_8O_{115.5}Si_3W_{28}$	$C_{14}H_{37}As_2Mn_3N_6Na_6O_{72}W_{18}$
Formula weight	3029.58	8774.21	5203.40
Crystal system	Monoclinic	Triclinic	Monoclinic
Space group	$C2/c$	$P\overline{1}$	$P2_1/c$
a (Å)	19.236(4)	15.364(3)	18.184(4)
b (Å)	17.942(4)	20.866(4)	32.085(6)
c (Å)	20.168(4)	30.156(6)	17.547(4)
α (°)	90	87.59(3)	90
β (°)	97.74(3)	87.04(3)	93.91(3)
γ (°)	90	87.15(3)	90
Volume (Å^3)	6897(2)	9635(3)	10214(4)
Z	4	2	4
Calculated density (Mg m^{-3})	2.918	3.024	3.384
Absorption coefficient (mm^{-1})	18.575	17.413	21.291
F(000)	5300	7832	9112
Goodness-of-fit on F^2	1.004	0.999	0.982
$R_1(I>2\sigma(I))$[a]	0.0691	0.0693	0.0783
wR_2[b]	0.1306	0.1495	0.1362

[a] $R_1 = \|F_0|-|F_c\|/|F_0|$.
[b] $wR_2 = [w(F_0^2-F_c^2)^2]/[w(F_0^2)^2]^{1/2}$.

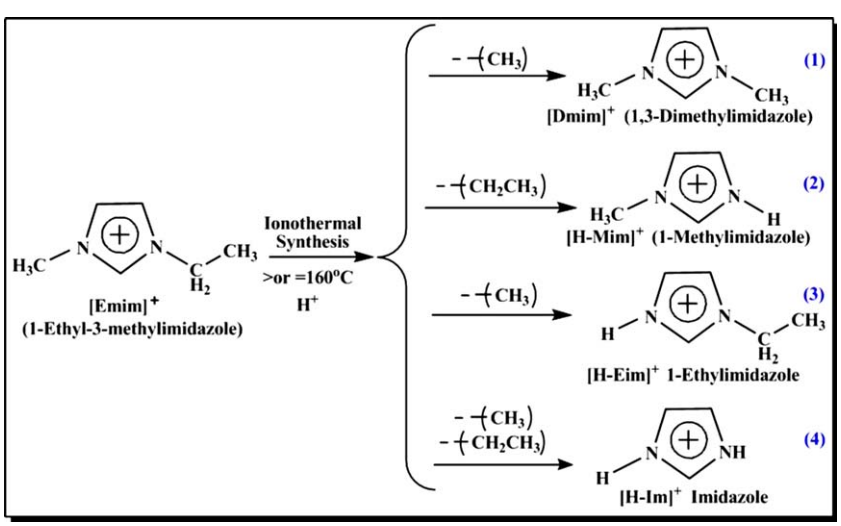

Scheme 1. The possible reaction products of the [Emim]$^+$ cations in the ionothermal synthesis.

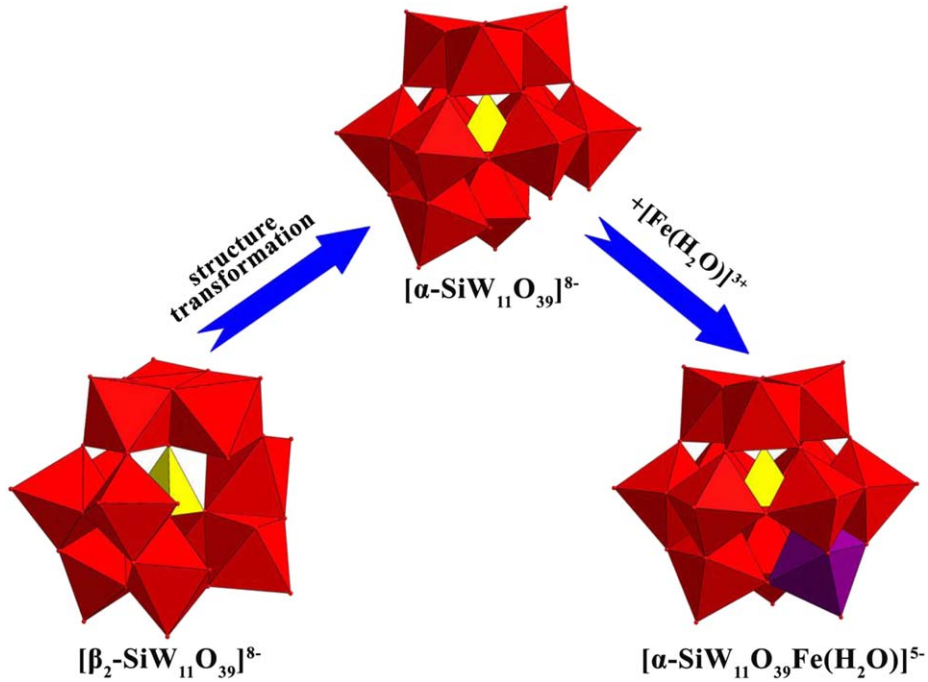

Fig. 1. Polyhedral representation of the structure of $[\alpha\text{-}SiW_{11}O_{39}]^{8-}$ unit derived from the $[\beta_2\text{-}SiW_{11}O_{39}]^{8-}$ unit and the coordination mode of Fe^{3+} on this monovacant Keggin-type building block in $[Dmim]_2Na_3[SiW_{11}O_{39}Fe(H_2O)]\cdot H_2O$ (**1**).

the syntheses of **1**–**3**. The $[Emim]^+$ cations may be partly decomposed to some new reaction products, the instability of the ILs may facilitate the reactions [8,28–30]. If the temperature is up to or more than 160 °C, four possible reaction products of the $[Emim]^+$ cations in the ionothermal synthesis are listed in Scheme 1, either they dissociate or coordinate to the crystal structures [8,28]. Products (2)–(4) may be protonated in the acidic conditions (Scheme 1). For the syntheses of **1**–**3**, products (1) and (2) dissociate around the polyoxoanions of **1** and **3**, while product (2) is protonated in **3**.

By means of the building block approach, the reactions of vacant heteropolyanions and transition metal cations in [Emim]Br result in the isolations of **1**–**3**. Three key factors should be emphasized in the ionothermal synthesis of **1**–**3**. Firstly, the molar ratio of the reactants and ILs should ensure that the reactants are adequately dissolved in [Emim]Br. Secondly, the reaction temperature may play an important role in the syntheses of **1**–**3**. If the reaction temperature is lower than 150 °C for **1**–**3**, no crystals could be obtained. Thirdly, the reaction time and the crystallization time are also crucial for the crystallizations. If the reaction time is more than 10 days, the viscosity of the IL will be too large to obtain crystal products under this condition. It is worthy to be mentioned that during the synthesis of **1**, $NaVO_3$ did not exist in the final structure of **1**. If $NaVO_3$ was not introduced into the reaction mixture, no crystal products were isolated under similar reaction conditions, so it may be presumed that $NaVO_3$ might be beneficial for obtaining the high quality crystals and enhancing the product yields of **1**. The similar synthesis phenomena also exist in the syntheses of other POMs [31–36]. In addition, under the heating condition, $[\beta_2\text{-}SiW_{11}O_{39}]^{8-}$ is inclined to transform to relatively stable polyanion $[\alpha\text{-}SiW_{11}O_{39}]^{8-}$, which indicate that $[\beta_2\text{-}SiW_{11}O_{39}]^{8-}$ possesses higher reaction activity than directly using $[\alpha\text{-}SiW_{11}O_{39}]^{8-}$. On the other hand, the strong ligand-to-metal charge transfer (LMCT) interactions finally result in the black color of **1**. For **2**, $Ce(NO_3)_3$ was introduced to synthesize the 3d–4f heterometallic aggregate under the ionothermal synthesis as we reported [37], but unfortunately, no Ce^{3+} cations were in the final structure of **2**. The parallel experiments demonstrated that if $Ce(NO_3)_3$ was not used in the reactions, compound **2** was still obtained, but the yield and crystal quality were greatly reduced [31–36]. For **3**, when the reaction mixture was stirred in air, the color of the mixture was observed from yellow to purple, which indicated that the Mn^{2+} cations had been oxidated to Mn^{3+} cations by $K_2S_2O_8$. After the mixture was reacted at 180 °C for six days, the color of the mixture was still purple, indicating that the Mn^{3+} cations were not changed under the ionothermal synthesis. Additionally, the synthesis of $Mn^{III/IV}$-substituted POMs is usually difficult owing to the high instability of these ions in aqueous solution. The successful obtainment of **3** indicates that the ionothermal synthesis system may fix the Mn^{III} ions into the POMs structures. Furthermore, the parallel experiments investigations reveal that compounds **1**–**3** were all stable in the range of 3.5–6.5.

3.2. Crystal structures of compounds 1–3

3.2.1. Structure of $[Dmim]_2Na_3[SiW_{11}O_{39}Fe(H_2O)]\cdot H_2O$ (**1**)

Single crystal X-ray diffraction analysis shows that **1** consists of a mono-iron^{III}-substituted α-Keggin polyoxoanion $[\alpha\text{-}SiW_{11}O_{39}Fe(H_2O)]^{5-}$, which is composed of a $[\alpha\text{-}SiW_{11}O_{39}]^{8-}$ moiety and a $[Fe(H_2O)]^{3+}$ unit (Figs. 1 and S1). Furthermore, there is a structure transformation from $[\beta_2\text{-}SiW_{11}O_{39}]^{8-}$ to $[\alpha\text{-}SiW_{11}O_{39}]^{8-}$ in the reaction process and the vacant site is filled with $[Fe(H_2O)]^{3+}$ unit (Fig. 1). In **1**, the Si atom exhibits a tetra-coordination environment. The Si–O distances vary from 1.51(3) to 1.68(2) Å and the O–Si–O angles from 64.3(15)° to 108.4(15)° (Table S1). And the Si1 atom is disordered with the occupancy of 50%, the atoms coordinated to Si1 are also disordered with the occupancies of 50%, separately (Figure S1b). All W centers represent octahedral environments. The W–O bond distances and the O–W–O bond angles are in the range of 1.625(14)–2.47(3) Å and 98.0(9)–160.5(11)° (Table S1). Furthermore, there are also site disorders in W2 (Fe2), W3 (Fe3), W4 (Fe4), W5 (Fe5) and W6 (Fe6) positions with the occupancies of 90% (10%), respectively (Figure S1a), finally resulting in 1 Fe and 11 W in the

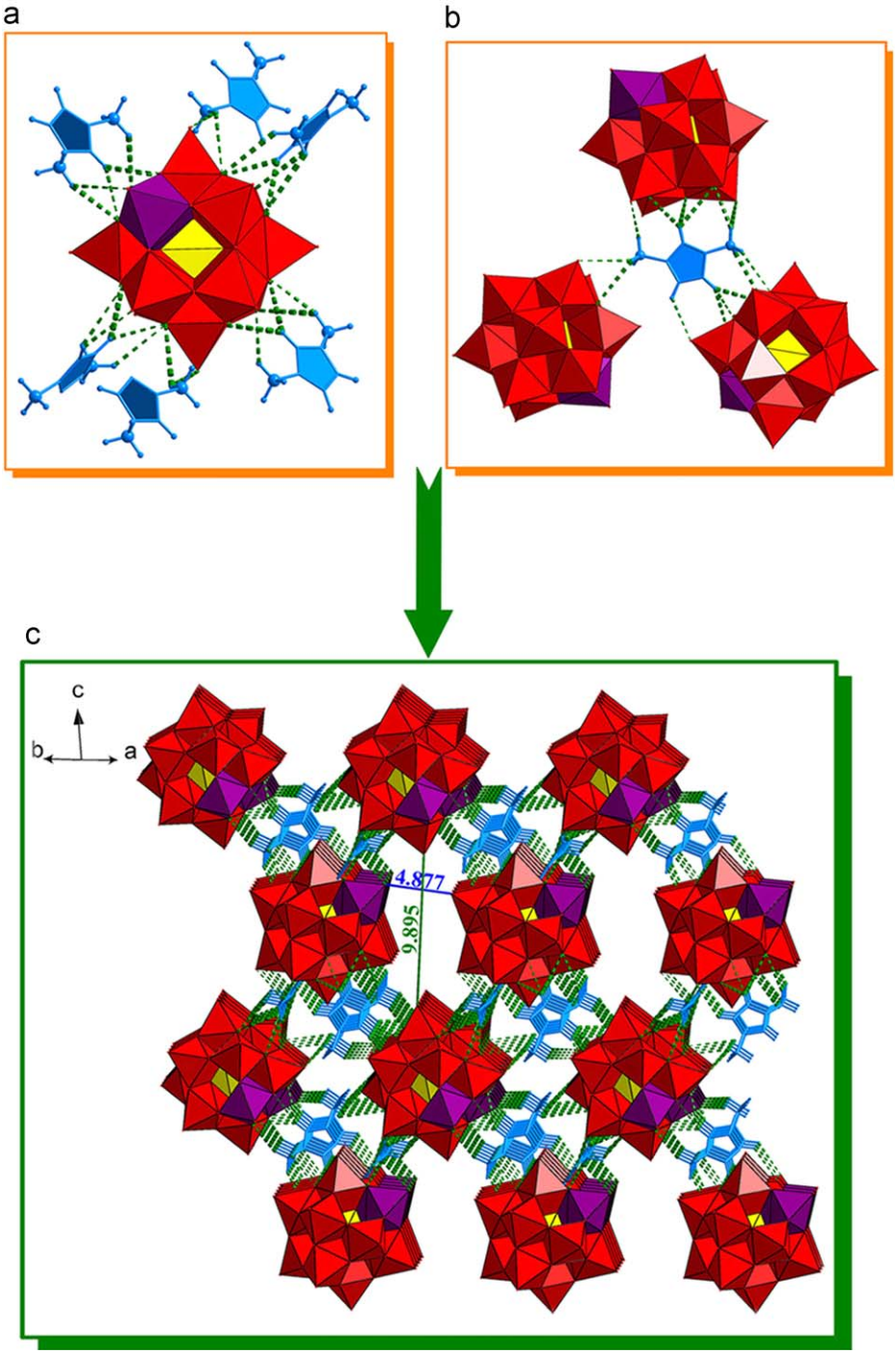

Fig. 2. (a) The coordination mode of hydrogen bonds around each polyoxoanion in $[Dmim]_2Na_3[SiW_{11}O_{39}Fe(H_2O)] \cdot H_2O$ (**1**), (b) The hydrogen bond coordination mode around each $[Dmim]^+$ cation in **1** and (c) The 3-D packing structure of **1** composed of hydrongen bonds viewed along (1, 1, 0) direction. The polyanions are represented with polyhedron.

12 sites. The polyanion in **1** possesses five negative charges, which are balanced by two dissociative, protonated $[Dmim]^+$ cations and three Na^+ cations. The BVS calculation results indicate that all Si, W and Fe sites possess +4, +6 and +3 oxidation states, respectively [38,39].

In the packing arrangement, the adjacent polyanions and the $[Dmim]^+$ cations of **1** are connected through hydrogen bonds to form a 3-D open-framework with 1-D tunnels both viewed from (1,1,0) (Fig. 2c) and (1,0,1) directions (Figure S2a). The hydrogen bonds are formed with the interactions between the hydrogen atoms coordinated to carbon atoms of $[Dmim]^+$ cations and the adjacent oxygen atoms of polyoxoanions in **1** with the mode of {C–H…O}. The hydrogen bond lengths are in the range of 2.478–3.091 Å. Each polyoxoanion is surrounded with six $[Dmim]^+$ cations through the hydrogen bonds (Fig. 2a), while each $[Dmim]^+$ cation is connected with three polyoxoanions via the hydrogen bonds (Fig. 2b). This type of connection modes result in the formations of the 1-D square tunnels. On the basis of the distances between the nearest and furthest terminal oxygen atoms of adjacent polyanions, the tunnel size is ca. 4.877 ×

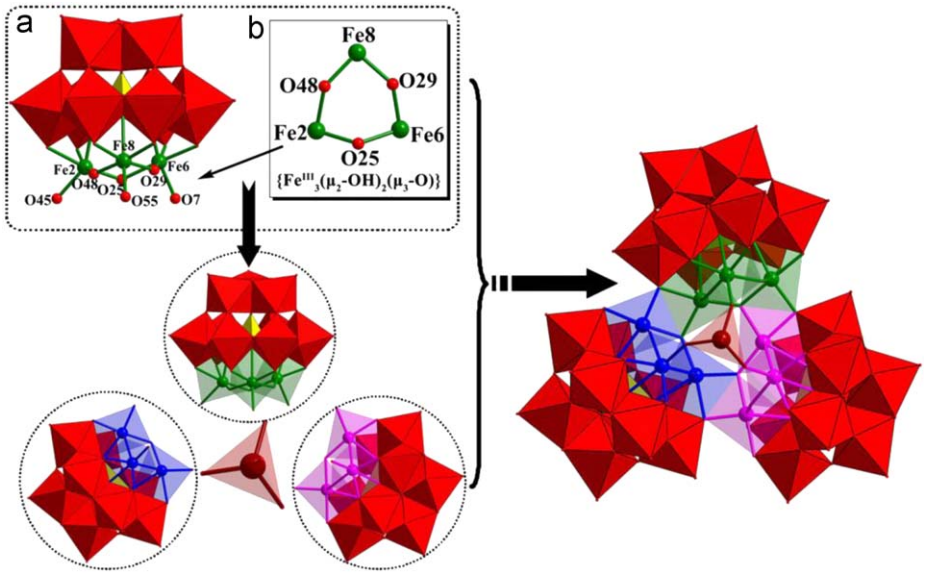

Fig. 3. The connection modes of the basic building blocks in $[Emim]_9Na_8[(SiW_9O_{34})_3\{Fe_3(\mu_2\text{-}OH)_2(\mu_3\text{-}O)\}_3(WO_4)]\cdot 0.5H_2O$ (**2**): (a) Polyhedral and ball-and-stick representation of the basic building blocks of **2**. (b) The ball-and-stick representation of the $\{Fe^{III}_3(\boldsymbol{\mu}_2\text{-}OH)_2(\boldsymbol{\mu}_3\text{-}O)\}$ moiety in **2**.

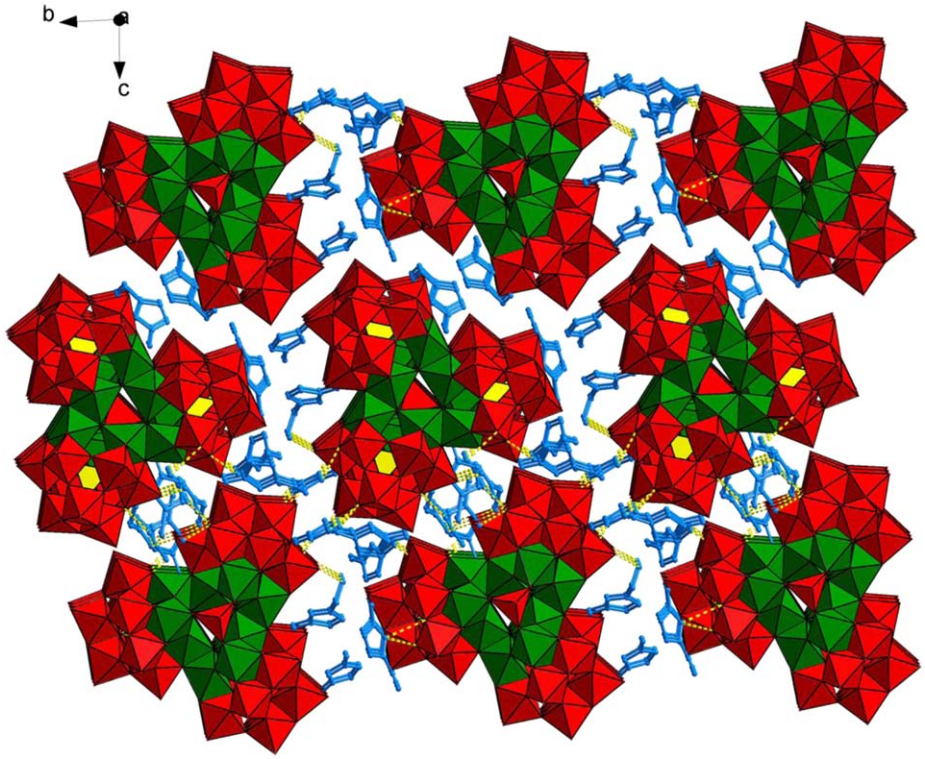

Fig. 4. The 3-D packing structure of $[Emim]_9Na_8[(SiW_9O_{34})_3\{Fe_3(\mu_2\text{-}OH)_2(\mu_3\text{-}O)\}_3(WO_4)]\cdot 0.5H_2O$ (**2**) composed of hydrongen bonds viewed along *a* axis. The polyanions are represented with polyhedra; all the hydrogen atoms are omitted for clarity.

9.895 Å viewed from (1,1,0) directions (Fig. 2c), while viewed from (1,0,1) directions, the tunnel size is ca. 15.407 × 30.787 Å (Figure S2a). The lattice water molecules and Na^+ cations in **1** were resided in the tunnels. Furthermore, from the topological view, the $[SiW_{11}O_{39}Fe(H_2O)]^{5-}$ polyoxoanion can be abstracted to be a four-connected node which links with four polyoxoanions. And the hydrogen bond linkers and $[Dmim]^+$ cations are rationalized as beelines. On the basis of the above connections, the 3-D open packing arrangement of **1** viewed from (1,0,1) direction can be abstracted into a 3-D four-connected net (Figure S2b).

3.2.2. *Structure of $[Emim]_9Na_8[(SiW_9O_{34})_3\{Fe_3(\mu_2\text{-}OH)_2(\mu_3\text{-}O)\}_3(WO_4)]\cdot 0.5H_2O$ (**2**)*

The polyoxoanion of **2** possesses an interesting cryptand-type structure constructed from three trinuclear-iron-cluster-substituted Keggin moieties $[\{Fe^{III}_3(\mu_2\text{-}OH)_2(\mu_3\text{-}O)\}(A\text{-}\alpha\text{-}SiW_9O_{34})]^{3-}$ ($\{Fe_3SiW_9\}$) and a $\{\mu_4\text{-}WO_4\}$ fragments (Figs. 3 and S3). In the cluster, all $\{Fe_3SiW_9\}$ units are composed of the trivacant Keggin $\{A\text{-}\alpha\text{-}SiW_9O_{34}\}$ building blocks and the $\{Fe^{III}_3(\mu_2\text{-}OH)_2(\mu_3\text{-}O)\}$ moieties. The W–O bond lengths vary from 1.68(2) to 2.45(2) Å and the O–W–O angles in the range of 96.5(8)–174.2(7)° (Table S2). The Fe–O bond lengths are in the range of 1.879(16)–

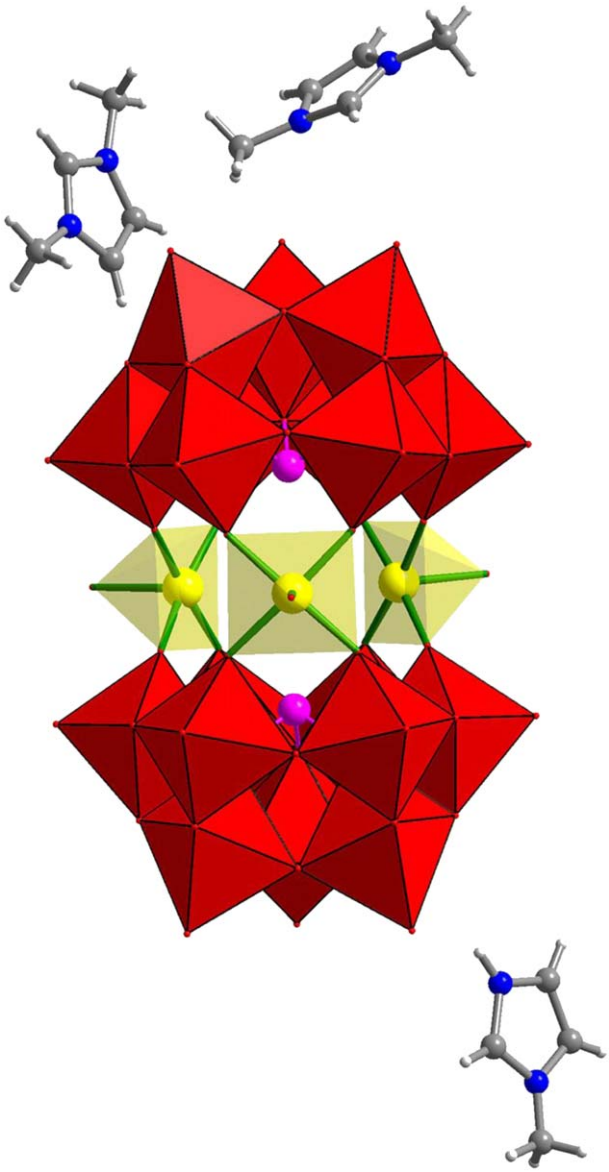

Fig. 5. Polyhedral and ball-and-stick representation of the polyoxoanion of $[Dmim]_2[HMim]Na_6[(AsW_9O_{33})_2\{Mn^{III}(H_2O)\}_3]\cdot 3H_2O$ (**3**).

2.328(15) Å, the O–Fe–O angles range from 77.2(7) to 171.0(8) Å. The BVS calculations indicate that the oxidation states of all W, Si and Fe centers are +6, +4 and +3, respectively (Tables S2 and S3) [38,39]. In the $\{Fe_3^{III}(\mu_2\text{-OH})_2(\mu_3\text{-O})\}$ moiety, Fe(8) center is coordinated with three terminal oxygen atoms derived from the $\{SiW_9O_{34}\}$ unit, two μ_2-OH bridges (O(48), O(29)) and one surface oxygen atom (O(55)) from one $\{\mu_4\text{-}WO_4\}$ unit, possessing a six-coordination environment. Fe(2) is also six-fold coordinated, which formed by three surface oxygen atoms from the $\{SiW_9O_{34}\}$ unit, two μ_3-OH bridges (O(45), O(48)) and one μ_3-O atoms (O(25)). Fe (6) center has the same coordination environments as Fe(2) (Figs. 3a, b and S4). The polyoxoanion of **2** can also be described as a $[\{Fe_3^{III}(\mu_2\text{-OH})_2(\mu_3\text{-O})\}_3(\mu_4\text{-}WO_4)]$ ($\{Fe_9^{III}W\}$) cluster surrounded by three $\{SiW_9\}$ POM ligands. In the $\{Fe_9^{III}W\}$ aggregate, the BVS values of the oxygen bridges indicate that the di-bridged oxygen atoms O(37), O(84), O(48), O(50), O(83) and O(29) are all the hydroxy oxygen atoms, while the tri-bridged oxygen atoms O(45), O(25) and O(12) are negative oxygen atoms [39] (Table S4 and Figure S4). The trimeric polyoxoanion of **2** possesses 17 negative charges charge-balanced by eight sodium cations and nine $[Emim]^+$ cations dissociating around the large polyoxoanions, which is consistent with the BVS calculation results. In the packing arrangement, the trimeric clusters and the $[Emim]^+$ cations are connected by hydrogen bonds into a 3-D open framework viewed along *a* axis (Fig. 4). The hydrogen bond lengths are in the range of 2.700–3.080 Å.

3.2.3. Structure of $[Dmim]_2[HMim]Na_6[(AsW_9O_{33})_2\{Mn^{III}(H_2O)\}_3]\cdot 3H_2O$ (3)

The polyanion of **3** consists of two $[\alpha\text{-}AsW_9O_{33}]^{9-}$ moieties linked together by three $\{Mn^{III}(H_2O)\}$ units via the W–O–Mn connection mode, leading to a sandwich-type structure (Fig. 5). The W–O bond lengths are in the range of 1.666(19)–2.42(2) Å and O–W–O bond angles vary from 96.5(10)° to 173.8(9)° (Table S5). All the W and Mn sites in the central sandwiched part exhibit a square-pyramid penta-coordination environment. The polyanion in **3** is charge-balanced by two dissociative $[Dmim]^+$ cations, one protonated $[H\text{-}Mim]^+$ cation and six sodium cations. The BVS calculations indicate that all As, W and Mn sites possess +3, +6 and +3 oxidation states, respectively (Table S6) [38,39]. In the packing arrangement, the adjacent sandwiching polyanions of **3** are connected by the hydrogen bonds among the dissociative $[Dmim]^+$ cations, protonated $[H\text{-}Mim]^+$ cations and the surface oxygen atoms of the polyoxoanions to form a 3-D open-framework viewed along *a* axis (Fig. 6). The hydrogen bond lengths range from 2.997 to 3.065 Å.

3.3. XRD, XPS and EPR analyses

In order to check the phase purities of **1–3**, the X-ray powder diffraction (XRD) patterns of **1–3** were recorded at room temperature. The peak positions of simulated (Figure S5a) and experimental (Figure S5b) patterns of **1**, the simulated (Figure S6a) and experimental (Figure S6b) patterns of **2**, as well as the simulated (Figure S7a) and experimental (Figure S7b) patterns of **3** are in agreement with each other, respectively, indicating the good phase purities of **1**, **2** and **3**. The differences in intensity may be due to the preferred orientations of the crystalline powder samples.

X-ray photoelectron spectrum (XPS) was recorded to identify the oxidation states of Mn centers in **3**. XPS for **3** (Fig. 7a) displays two peaks of ca. 653.7 and ca. 641.5 eV in the energy regions of $Mn2p_{1/2}$ and $Mn2p_{3/2}$ separately [40]. The result is in agreement with the BVS calculations. In the electron paramagnetic resonance (EPR) spectrum of **3** (Fig. 7b), two signals at about g_1=2.2789 (2966G) and g_2=2.0011 (3227G) are observed, as expected for manganese (III) systems [41]. (Fig. 7b) The value of g_1 is a little higher than the g values for three isolated spin-only Mn^{3+} ions (considering S=2), which may be caused by the zero-field splitting effect and the weak spin-orbit coupling [42,43]. The EPR results of **3** indicate that the Mn^{3+} ions are in the high-spin state with four unpaired electrons. However, it only permit a qualitative characterization because of the spectroscopic complexities of high-spin Mn^{3+} compared with the orbital degeneracy of the ground state and changeable coupling of excited-state terms in the coordination environment.

3.4. The stability studies of 1–3

TG-DTA analyses were aimed to determine the thermal stabilities of **1–3**. The investigations indicate that the initial decomposition temperatures of the organic cations in **1–3** are 320 °C for **1**, 348.1 °C for **2** and 291 °C for **3**, separately, while those of the polyoxoanions in **1–3** are 557.4 °C for **1**, 531.5 °C for **2** and

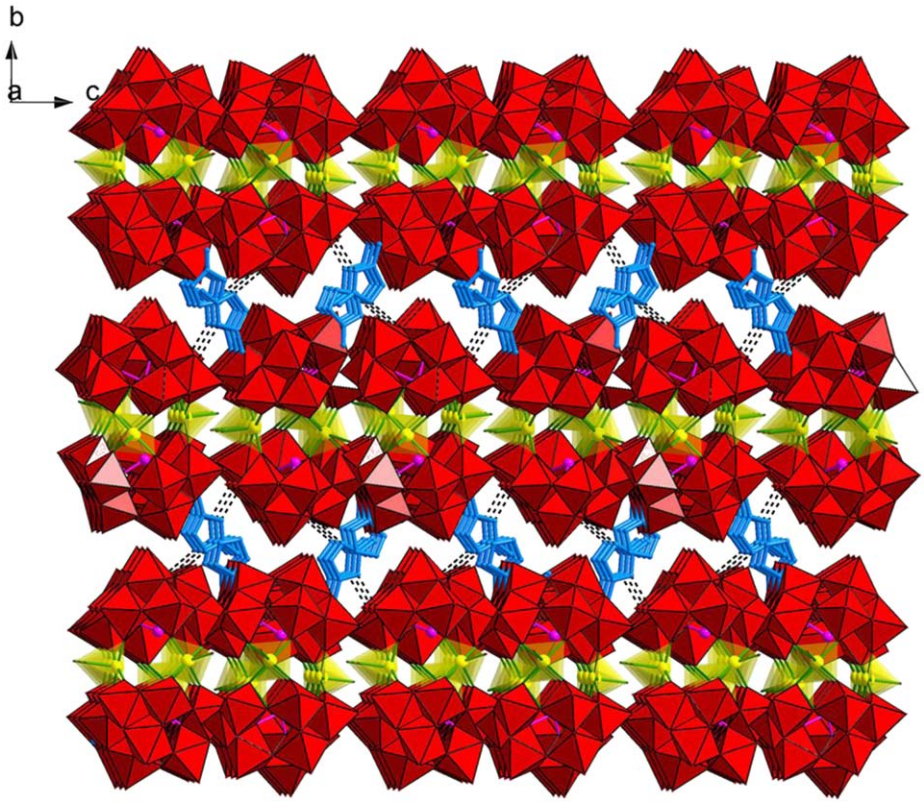

Fig. 6. The 3-D packing structure of $[Dmim]_2[HMim]Na_6[(AsW_9O_{33})_2\{Mn^{III}(H_2O)\}_3]\cdot 3H_2O$ (**3**) composed of hydrongen bonds viewed along *a* axis. The polyanions are represented with polyhedra; all the hydrogen atoms are omitted for clarity.

550 °C for **3**, respectively (Figure S8 for 1, Figure S9 for 2 and Figure S10 for 3).

The stabilities of **1**–**3** in the solutions were also studied. *Firstly*, the solid state UV–vis spectra and solution UV–vis spectra of **1–3** were measured. The three types of characteristic peaks in the solid state spectra of **1** (Figure S11a), **2** (Figure S12a) and **3** (Figure S13a) also exist in their solution spectra of **1** (Figure S11b), **2** (Figure S12b) and **3** (Figure S13b), respectively, which indicate that the polyoxoanions of **1**, **2** and **3** still keep their structures in the solutions [44–47]. Simultaneously, the solution UV–vis spectra of **1–3** are virtually unchanged with time (Figure S11b for 1, Figure S12b for 2 and Figure S13b for 3), also indicating that the polyoxoanions of **1–3** are stable in the solutions [44–47]. It is worthy to mention that the peak positions of the solution UV–vis spectra are a little different from that of the solid state spectra in **1**–**3** only with some peak shifts, which may be ascribed to their different testing methods and conditions. *Secondly*, the CVs for **1–3** studied in $0.5\,M\cdot H_2SO_4/Na_2SO_4$ (pH=4.50) at different scan rates also indicate that the polyanions of **1**–**3** are stable in the solutions (Figure S14). *Thirdly*, the stability of **2** in the solution was also estimated by the gel filtration chromatography [48], the analysis reveals that **2** elutes faster than $[P_2W_{15}Mo_2VO_{62}]^{8-}$ (**2a**) (ionic mass=4055), indicating that the molecular mass of **2** (ionic mass=7580) is quite different from that of **2a** and rules out the possibility of **2** breaking down into one dimer, one monomer and mixtures of the two. If polyoxoanions **2** were indeed the dimers in the solution, they have ionic masses of 3790 g/mol, a little lower than that of **2a**, which would elute slightly later. If polyoxoanions **2** fall apart, resulting in monomers, they have the ionic masses of 2527, and therefore would elute later. As shown in the photograph of the Sephadex G-50 column, two distinct colored bands corresponding to **2a** (dark blue) and **2** (yellow) have already been separated (Figure S15). The experiment confirms that polyoxoanion **2** still keeps the trimeric structures in aqueous solutions.

The TG-DTA, XRD, and N_2 adsorption measurements of **1** were carried out to examine if the porous network of **1** is stable. According to the TG-DTA analysis results of **1**, the XRD patterns of **1** were checked at 20, 80 and 160 °C shown in Fig. 8, the peak positions of simulated and experimental XRD patterns at 20 °C are in agreement with each other, indicating the good phase purity of **1**. However, most peaks of the XRD pattern of **1** disappear at 80 and 160 °C, suggesting that **1** has not been the crystalline state and the framework might be collapsed with the loss of the coordinated water molecules. Although the structure seems to be still stable before 256 °C from the TG curve, the three wide endothermal peaks observed at 66.1, 94.2 and 192.7 °C in the DTA curve, which indicate that the organic cations $[Dmim]^+$ may be rearranged in the porous structure of **1** during the endothermal process, resulting in the collapses of the porous framework. In addition, the N_2 sorption isotherm of **1** at 77 K reveals that the adsorption and desorption curves are almost superposition (Figure S16). The BET surface area is only $50.81\,m^2g^{-1}$ and the maximum N_2 uptake is only $28.13\,cm^3g^{-1}$ reached at 1 atm. It may be only the physical adsorption but not the chemical adsorption. Herein, the porous network of **1** is not stable when it is heated.

3.5. Electrochemical and electrocatalytic activities

In order to study the redox properties of **1**–**3**, the electrochemical behaviors of **1**, **2** and **3** were studied in $0.5\,M\cdot H_2SO_4/Na_2SO_4$ (pH=4.50) aqueous solutions. The CV of **1** (Fig. 9a) shows two reversible peaks at $E_{1/2}=(E_{pa}+E_{pc})/2 = -667$ mV (I/I′) and +43.5 mV (II/II′), corresponding to the W^{VI} redox processes [49,50] and a reversible peak at $E_{1/2} = +512$ mV (III/III′), indicating the Fe^{III} redox process, which further proves the existence of Fe^{3+} in **1** [50–52]. Anson et al. have ever reported the electrochemistry of

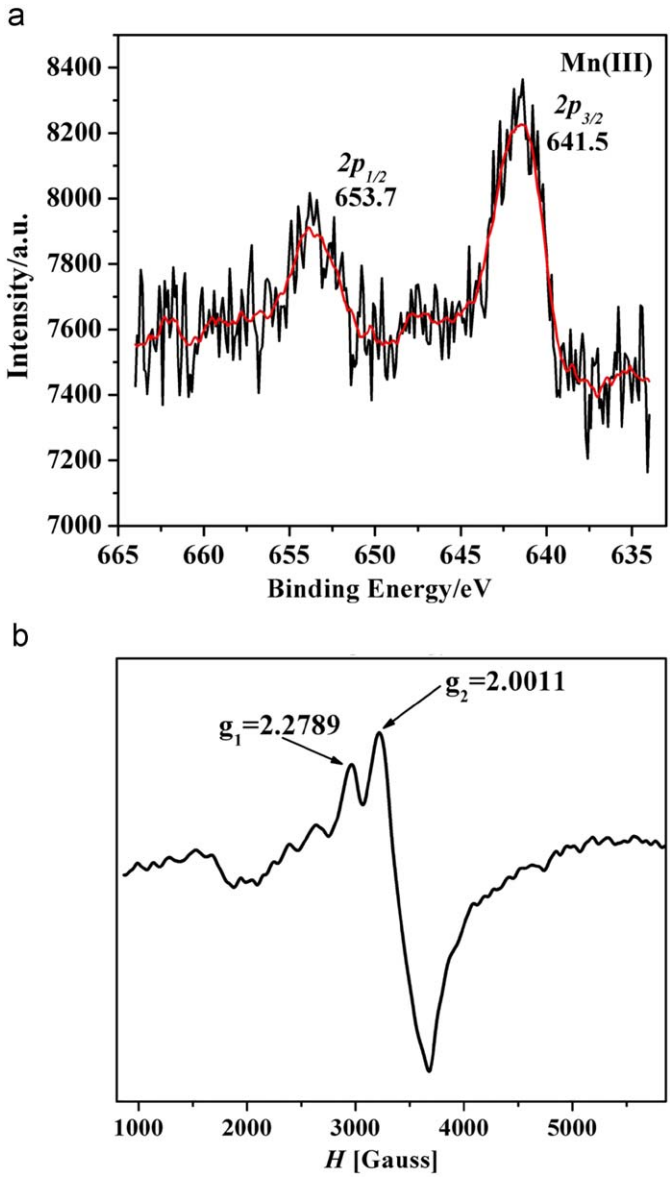

Fig. 7. (a) The XPS spectra of Mn(III) in $[Dmim]_2[HMim]Na_6[(AsW_9O_{33})_2\{Mn^{III}(H_2O)\}_3]\cdot 3H_2O$ (**3**) and (b) The EPR spectrum of **3**.

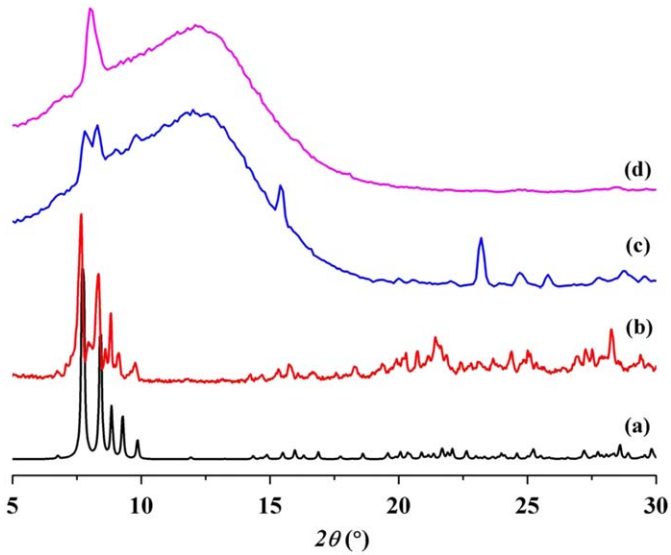

Fig. 8. Stimulated and experimental XRD patterns of **1**. (a) stimulated XRD, (b) XRD at 20 °C, (c) XRD at 80 °C, and (d) XRD at 160 °C.

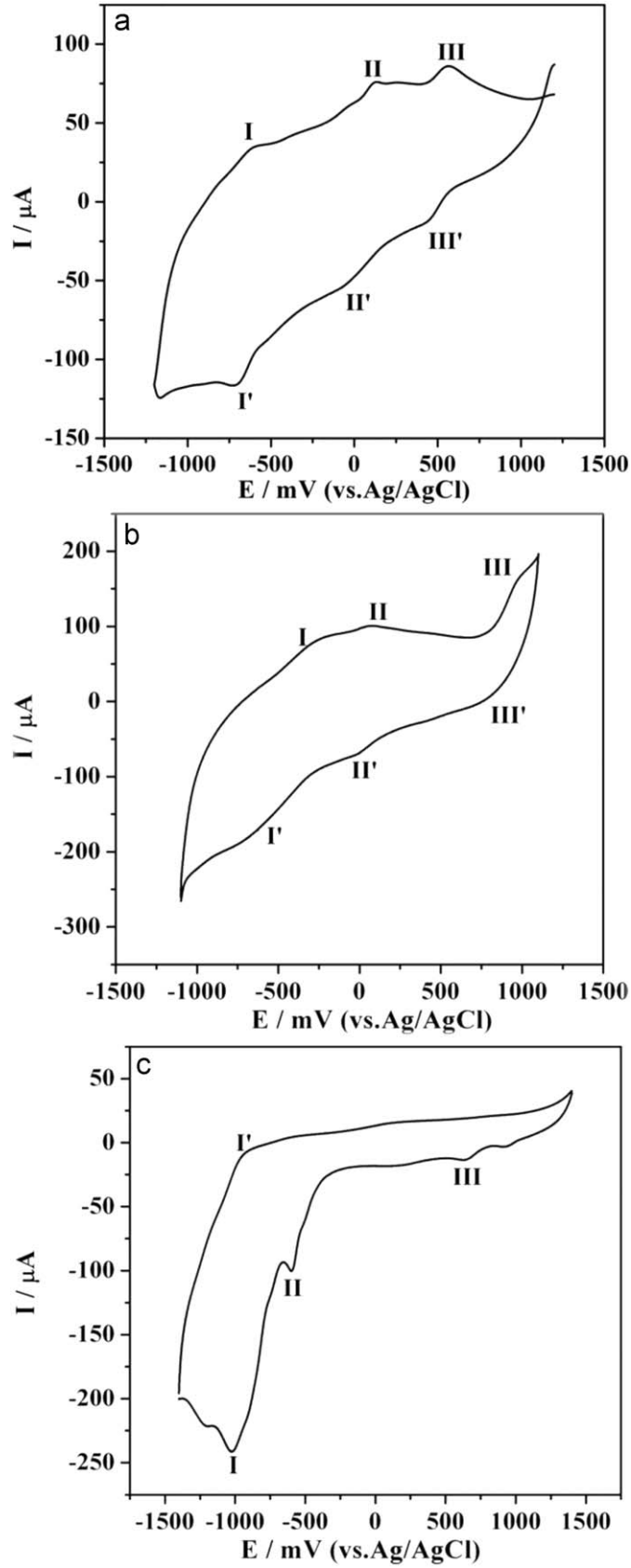

Fig. 9. CVs for 1 mM sample of $[Dmim]_2Na_3[SiW_{11}O_{39}Fe(H_2O)]\cdot H_2O$ (**1**) (**a**), $[Emim]_9Na_8[(SiW_9O_{34})_3\{Fe_3(\mu_2\text{-}OH)_2(\mu_3\text{-}O)\}_3(WO_4)]\cdot 0.5H_2O$ (**2**) (**b**) and $[Dmim]_2[HMim]Na_6[(AsW_9O_{33})_2\{Mn^{III}(H_2O)\}_3]\cdot 3H_2O$ (**3**) (**c**) in 0.5 M H_2SO_4/Na_2SO_4 (pH=4.50) solutions. Working electrode: glassy carbon, Reference electrode: Ag/AgCl, Scan rate: 50 mVs^{-1}.

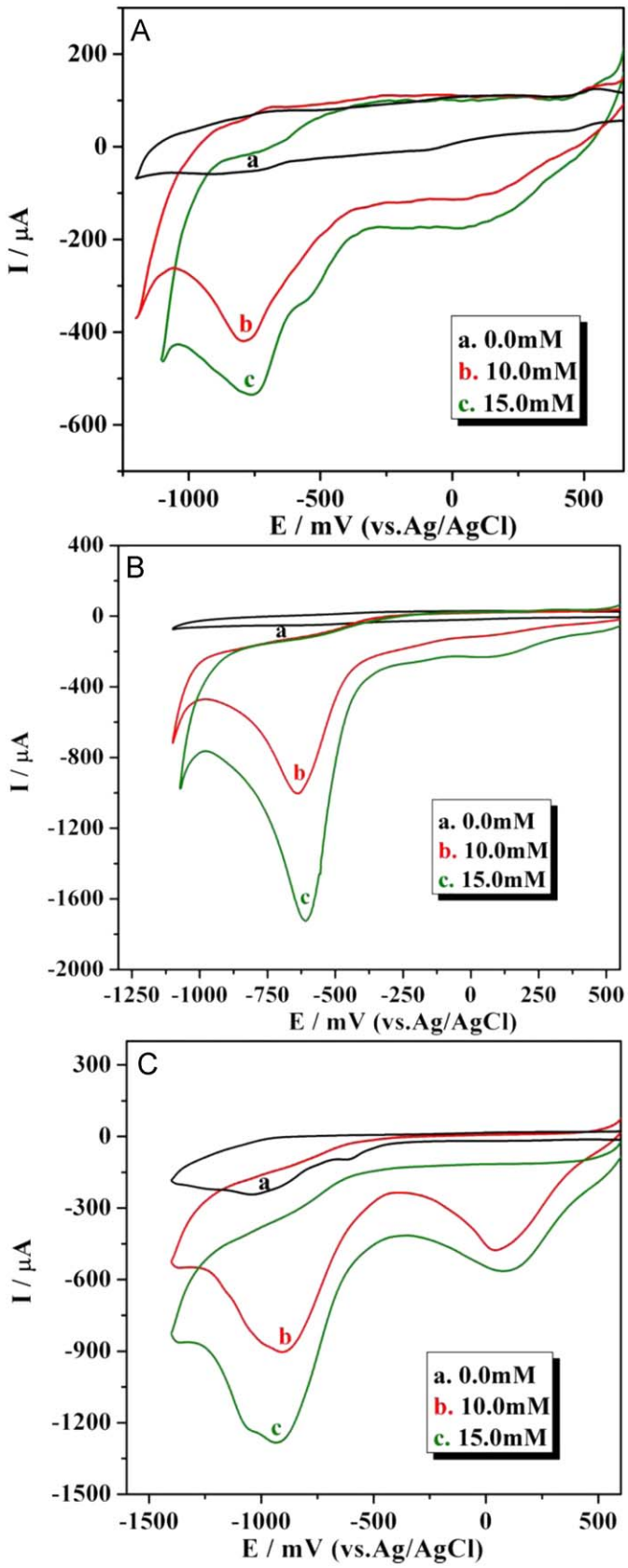

Fig. 10. Electrocatalytic reduction of NO_2^- in 1 mM 0.5 M H_2SO_4/Na_2SO_4 solutions of $[Dmim]_2Na_3[SiW_{11}O_{39}Fe(H_2O)]\cdot H_2O$ (**1**) (**A**), $[Emim]_9Na_8[(SiW_9O_{34})_3\{Fe_3(\mu_2\text{-}OH)_2(\mu_3\text{-}O)\}_3(WO_4)]\cdots 0.5H_2O$ (**2**) (**B**) and $[Dmim]_2[HMim]Na_6[(AsW_9O_{33})_2\{Mn^{III}(H_2O)\}_3]\cdot 3H_2O$ (**3**) (**C**), at a scan rate of 50 mV s^{-1}, containing NO_2^- concentrations of 0.0 (a), 10.0 (b) and 15.0 (c) mM.

$K_5[SiFe^{III}(H_2O)W_{11}O_{39}]$ (**1a**) [53], compared to the CV of **1a**, the intensities of three pairs of peak in the CV of **1** greatly decrease and all the peak positions shift to the lower potentials. It may be ascribed to the different CV media with various concentrations in their electrochemical measurements [54–57]. The CV medium of **1** is 0.5 M · H_2SO_4/Na_2SO_4 (pH=4.50) aqueous solution, while that of **1a** is 0.1 M $NaClO_4$/0.01 M$HClO_4$ solution. In addition, the cations of **1** and **1a** are different, there are large organic cations $[Dmim]^+$ dissociating around the polyoxoanions in the CV medium of **1**, which may further slower the electron transfer process in the CV.

The CV of **2** (Fig. 9b) shows two redox pairs at $E_{1/2}=-452$ mV (I/I′) and +17.5 (II/II′) mV, which are responsible for the redox processes of W^{VI} in the polyoxoanion framework of **2** as reported [49,50] while redox peaks at $E_{1/2}$ = +898 mV (III/III′) is attributed to the Fe(III)/Fe(II) redox process [50–52]. The weak peak intensities of **2** in Fig. 9b are also caused by the slow electron transfer process of the W and Fe centers in **2**. The most significant point is

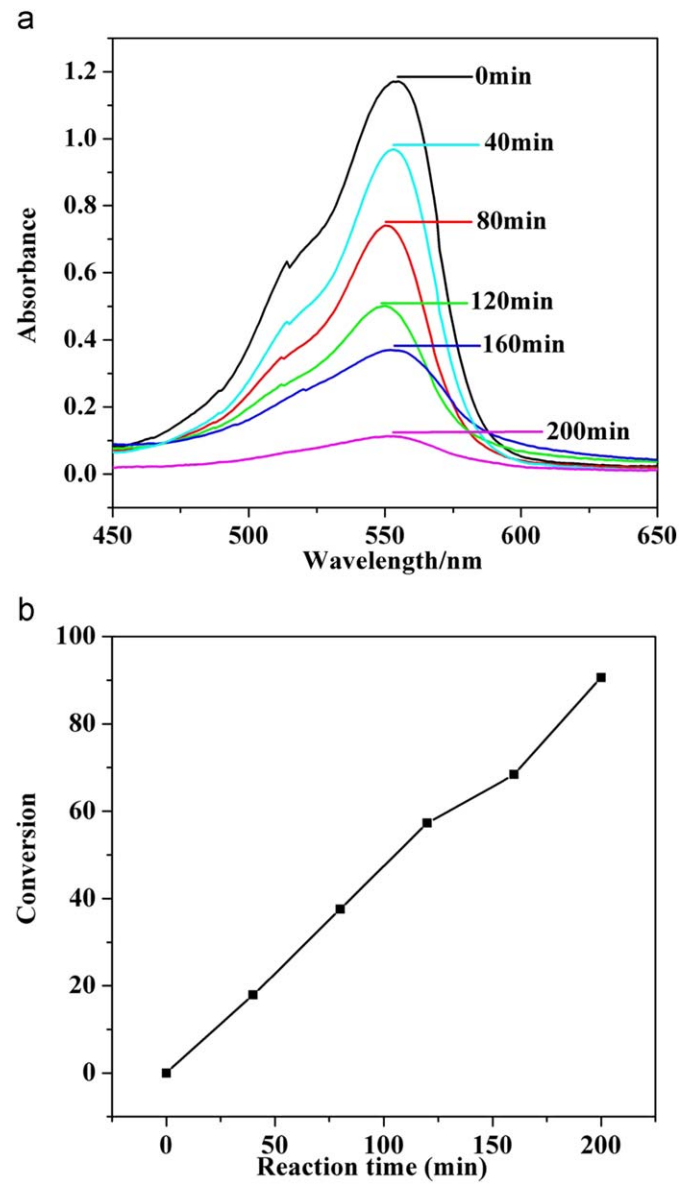

Fig. 11. (a) The UV–vis absorption spectra change of **2** recorded at a 0.5 M H_2SO_4/Na_2SO_4 solution at pH=4.50 including 2×10^{-4} M **2** and 2×10^{-5} M RhB and (b) Plot of the conversions of RhB versus reaction time for the photocatalyzer solutions of samples **1**–**3**.

that the redox peaks of Fe(III)/Fe(II) in **1** and **2** are different, which may be due to the different chemical environments of Fe centers in **1** and **2**. Compared to the structure of **1**, the more complicated coordination environments around the Fe centers in **2** may lead to the slower electron transfer processes, finally resulting in the weak peak intensities and higher peak positions.

For **3**, the CV (Fig. 9c) shows one pseudo-reversible peaks at $E_{1/2}$=−978 mV (I/I′) and a irreversible anodic peak at −608 mV (II) attributed to the W^{VI} redox processes [49,50] as well as one weak anodic peak at +635 mV (III) assigned to the Mn^{III} redox process [58–61]. Such type of CV feature about **3** probably result from slow electron transfer rather than chemical irreversibility. In our previous work, the electrochemical behavior of a structural analog $(C_6H_5NO_2)_4\{Mn^{III}(H_2O)\}[As^{III}W_9O_{33}]_2\{W(OH)\}\{W(H_2O)\}\cdot 18H_2O$ (**3a**) was investigated in $0.5\,M\cdot H_2SO_4/Na_2SO_4$ solution at pH=2.0 [62]. Its CV shows two similar reversible W^{VI} redox peaks and one irreversible anodic peak of Mn^{III} at +327 mV. The differences between the CV of **3** and **3a** are also mainly focused on the peak intensities and the peak positions. Their different measure conditions with different pH values may be the probable reasons [54–57].

It is well known that POMs are able to deliver the electrons to other species, thus serving as powerful electron reservoirs for multi-electron reductions. This property has been investigated extensively in electrocatalytic reductions. In numerous POMs structures, the polyoxoanions containing transition metal ions are favorable in the electrocatalytic processes [63]. In our experiment, we found that **1–3** present excellent electrocatalytic activity toward the reduction of nitrite. No obvious voltammetric response is obtained in the potential range for nitrite at the GC electrode in the absence of POMs [64]. For **1**, with the addition of nitrite, the pH value of the solution was changed, the two reduction peaks (I′ and II′) of W^{VI} combine to one wide strong peak (I′+II′) (Fig. 10a). The reduction peak currents of the incorporate tungsten waves increase dramatically, suggesting that the NO_2^- anions are reduced by the reduced species of the polyoxoanions, furthermore, the peak positions of Fe^{III} are shifted to the lower potentials and their the reduction peak (III′) currents also increase, which indicate that **1** displays electrocatalytic activity toward the reduction of nitrite (Fig. 10a) [50]. For **2** (Fig. 10b) and **3** (Fig. 10c), the tungsten waves also merge and the reduction peak currents of W^{VI} and Fe^{III} centers in **2**, the W^{VI} and Mn^{III} centers in **3** enhance sharply, indicating that **2** and **3** also exhibit electrocatalytic activities [50].

3.6. Photocatalytic activities of 1–3

The photocatalytic activities of **1–3** were investigated with photocatalytic degradations of rhodamine-B (RhB). The photocatalytic activity discussion of **2** is taken for example and the other compounds are in brief. The monitored UV–vis spectra of RhB using **2** as the photocatalyst indicate that the UV–vis intensities of RhB decrease obviously upon irradiation, confirming the photocatalytic property of **2** [65,66] (Fig. 11a). Simultaneously, compounds **1** and **3** also reveal photocatalytic activities (Figures S17 and S18). Moreover, the concentrations of RhB (K) versus reaction time (t) of samples **1–3** were plotted in Fig. 11b. The conversion of RhB (K) can be expressed as $K=(I_0-I_t)/I_0$, where I_0 represents the UV–vis intensity of RhB at the original reaction (t=0), while I_t is the UV–vis absorption intensity at a certain irradiation time t [67,68]. The calculation results show that the conversion of RhB using **2** as the photocatalyst is 90.6% during 200 min irradiation time, while those of **1** and **3** are 66.4% and 69.2%, respectively (Fig. 11b).

4. Conclusion

In summary, we have successfully synthesized three new transition-metal-containing polyoxotungstate hybrids via the ionothermal synthesis. The successful obtainments of compounds **1–3** prove that the ionothermal synthesis is a suitable synthesis method to construct the POMs-based aggregates. Compounds **1–3** show the photocatalytic and electrocatalytic properties. The continuing efforts will be paid on the synthesis of new POMs-based aggregates with other linking units such as various carboxylate ligands or lanthanide ions under ionothermal conditions.

Supporting information available

CCDC-734482 (for **1**), -734483 (for **2**) and -734484 (for **3**) contain the supplementary crystallographic data for this paper. These data can be obtained free of charge at http://www.ccdc.cam.ac.uk/conts/retrieving.html (or from the Cambridge Crystallographic Data Centre, 12, Union Road, Cambridge CB2 1EZ, UK; fax: +44-1223/336-033; E-mail: http://www.deposit@ccdc.cam.ac.uk). Ball-and-stick views of the structures of **1** and **2**, IR and TG-DTA curves of **1-3**. The diffuse reflectance and solution UV–vis spectra of **1–3**. XRD patterns of **1–3**. Photograph of the Sephadex G-50 column of **2**. The UV–vis absorption spectra changes of RhB in **1** and **3**. Gas sorption isotherm of **1** for N_2. Selected bond lengths and angles of **1–3**. Tables of the BVS of Fe, μ_2-OH and μ_3-O atoms in **2**, the BVS of Mn in **3**.

Acknowledgments

This work was supported by the National Natural Science Foundation of China (Nos. 20701005/20701006), the Science and Technology Development Project Foundation of Jilin Province (No. 20060420), the Postdoctoral Station Foundation of Ministry of Education (No. 20060200002), the Testing Foundation of Northeast Normal University (NENU), Science and Technology Creation Foundation of NENU (NENU-STC07009) and Science Foundation for Young Teachers of NENU (Nos. 20070302/20070312), the Program for Changjiang Scholars and Innovative Research Team in University.

Appendix A. Supplementary material

Supplementary data associated with this article can be found in the online version at doi:10.1016/j.jssc.2009.11.016.

References

[1] A. Müller, Y.S. Zhou, H. Bögge, M. Schmidtmann, T. Mitra, E.T.K. Haupt, A. Berkle, Angew. Chem. Int. Ed. 45 (2006) 460–465.
[2] J.D. Compain, P. Mialane, A. Dolbecq, I.M. Mbomekallé, J. Marrot, F. Sécheresse, E. Riviére, G. Rogez, W. Wernsdorfer, Angew. Chem. Int. Ed. 48 (2009) 3077–3081.
[3] C.P. Pradeep, D.L. Long, C. Streb, L. Cronin, J. Am. Chem. Soc. 130 (2008) 14946–14947.
[4] S.T. Zheng, J. Zhang, G.Y. Yang, Angew. Chem. Int. Ed. 47 (2008) 3909–3913.
[5] B.S. Bassil, M.H. Dickman, I. Römer, B. Von Der Kammer, U. Kortz, Angew. Chem. Int. Ed. 46 (2007) 6192–6195.
[6] Y. Hou, X.L. Fang, C.L. Hill, Chem. Eur. J. 13 (2007) 9442–9447.
[7] P. Wasserscheid, W. Keim, Angew. Chem. Int. Ed. 39 (2000) 3772–3789.
[8] R.E. Morris, Chem. Commun. (2009) 2990–2998.
[9] E.R. Cooper, C.D. Andrews, P.S. Wheatley, P.B. Webb, P. Wormald, R.E. Morris, Nature 430 (2004) 1012–1016.
[10] E.R. Parnham, R.E. Morris, J. Am. Chem. Soc. 128 (2006) 2204–2205.

[11] Z.J. Lin, D.S. Wragg, J.E. Warren, R.E. Morris, J. Am. Chem. Soc. 129 (2007) 10334–10335.
[12] W.M. Reichert, J.D. Holbrey, K.B. Vigour, T.D. Morgan, G.A. Broker, R.D. Rogers, Chem. Commun. (2006) 4767–4779.
[13] Z. Lin, A.M.Z. Slawin, R.E. Morris, J. Am. Chem. Soc. 129 (2007) 4880–4881.
[14] Z.J. Lin, Y. Li, A.M.Z. Slawin, R.E. Morris, Dalton Trans. (2008) 3989–3994.
[15] Z. Lin, D.S. Wragg, R.E. Morris, Chem. Commun. (2006) 2021–2023.
[16] Z. Li, Q. Zhang, H. Liu, P. He, X. Xu, J. Li, J. Power Sources 158 (2006) 103–109.
[17] L. Dai, S. Yu, Y. Shan, M. He, Eur. J. Inorg. Chem. (2004) 237–241.
[18] J. Kim, S. Hayashi, T. Mori, I. Honma, Electrochim. Acta 53 (2007) 963–967.
[19] N. Zou, W.L. Chen, Y.G. Li, W.L. Liu, E.B. Wang, Inorg. Chem. Commun. 11 (2008) 1367–1370.
[20] S.V. Dzyuba, R.A. Bartsch, J. Heterocycl. Chem. 38 (2001) 265–268.
[21] A. Tézé, G. Hervé, Inorg. Synth. 27 (1990) 91–92.
[22] A. Tézé, G. Hervé, Inorg. Synth. 27 (1990) 87–88.
[23] C. Tourné, A. Revel, G. Tourné, M. Vendrell, C.R. Acad. Soc. Paris Ser. C 277 (1973) 643–644.
[24] G.M. Sheldrick, SHELXL97, Program for Crystal Structure Refinement, University of Göttingen, Germany, 1997.
[25] G.M. Sheldrick, SHELXS97, Program for Crystal Structure Solution, University of Göttingen, Germany, 1997.
[26] G.R. Rao, T. Rajkumar, B. Varghese, Solid State Sci. 11 (2009) 36–42.
[27] T. Rajkumar, G.R. Rao, Mater. Lett. 62 (2008) 4134–4136.
[28] P.J. Byrne, D.S. Wragg, J.E. Warren, R.E. Morris, Dalton Trans (2009) 795–799.
[29] E.R. Parnham, R.E. Morris, Chem. Mater. 18 (2006) 4882–4887.
[30] E.R. Parnham, E.A. Drylie, P.S. Wheatley, A.M.Z. Slawin, R.E. Morris, Angew. Chem. Int. Ed. 45 (2006) 4962–4966.
[31] P. Mialane, A. Dolbecq, J. Marrot, E. Rivère, F. Sécheresse, Angew. Chem. Int. Ed. 42 (2003) 3523–3526.
[32] H.N. Miras, J. Yan, D.L. Long, L. Cronin, Angew. Chem. Int. Ed. (2008) 8420–8423.
[33] X.T. Zhang, D.Q. Wang, J.M. Dou, S.S. Yan, X.X. Yao, J.Z. Jiang, Inorg. Chem. 45 (2006) 10629–10635.
[34] Z.M. Zhang, Y.F. Qi, C. Qin, Y.G. Li, E.B. Wang, X.L. Wang, Z.M. Su, L. Xu, Inorg. Chem. 46 (2007) 8162–8169.
[35] W.L. Chen, Y.G. Li, Y.H. Wang, E.B. Wang, Eur. J. Inorg. Chem. (2007) 2216–2220.
[36] W.L. Chen, Y.G. Li, Y.H. Wang, E.B. Wang, Z.M. Su, Dalton Trans. (2007) 4293–4301.
[37] W.L. Chen, Y.G. Li, Y.H. Wang, E.B. Wang, Z.M. Zhang, Dalton Trans. (2008) 865–867.
[38] I.D. Brown, D. Altermatt, Acta Crystallogr. B 41 (1985) 244–247.
[39] W.T. Liu, H.H. Thorp, Inorg. Chem. 32 (1993) 4102–4105.
[40] Y.F. Han, F.X. Chen, Z.Y. Zhong, K. Ramesh, L.W. Chen, E. Widjaja, J. Phys. Chem. B 110 (2006) 24450–24456.
[41] K.A. Campbell, M.R. Lashley, J.K. Wyatt, M.H. Nantz, R.D. Britt, J. Am. Chem. Soc. 123 (2001) 5710–5719.
[42] J.P. Wang, P.T. Ma, J. Li, H.Y. Niu, J.Y. Niu, Chem. Asian J. 3 (2008) 822–833.
[43] J. Owen, E. A. Harris, Electron Paramagnetic Resonance, in: S. Geshwind, (Ed.), Plenum, New York, 1972, pp. 427–492.
[44] B.S. Bassil, S. Nellutla, U. Kortz, A.C. Stowe, J. van Tol, N.S. Dalal, B. Keita, L. Nadjo, Inorg. Chem. 44 (2005) 2659–2665.
[45] H.Y. An, E.B. Wang, D.R. Xiao, Y.G. Li, Z.M. Su, L. Xu, Angew. Chem. Int. Ed. 45 (2006) 904–908.
[46] L.H. Bi, U. Kortz, Inorg. Chem. 43 (2004) 7961–7962.
[47] L.H. Bi, U. Kortz, S. Nellutla, A.C. Stowe, J. van Tol, N.S. Dalal, B. Keita, L. Nadjo, Inorg. Chem. 44 (2005) 896–903.
[48] D.L. Nelson, M.M. Cox, A.L. Lehninger, Principles of Biochemistry, third ed., Worth Publishers, New York, 2000.
[49] B. Keita, I.M. Mbomekalle, L. Nadjo, R. Contant, Electrochem. Commun. 3 (2001) 267–273.
[50] B. Keita, I.M. Mbomekalle, Y.W. Lu, L. Nadjo, P. Berthet, T.M. Anderson, C.L. Hill, Eur. J. Inorg. Chem. (2004) 3462–3475.
[51] B. Godin, Y.G. Chen, J. Vaissermann, L. Ruhlmann, M. Verdaguer, P. Gouzerh, Angew. Chem. Int. Ed. 44 (2005) 3072–3075.
[52] L.H. Bi, U. Kortz, S. Nellutla, A.C. Stowe, J. van Tol, N.S. Dalal, B. Keita, L. Nadjo, Inorg. Chem. 44 (2005) 896–903.
[53] J.E. Toth, F.C. Anson, J. Am. Chem. Soc. 111 (1989) 2444–2451.
[54] B.S. Bassil, S. Nellutla, U. Kortz, A.C. Stowe, J. van Tol, N.S. Dalal, B. Keita, L. Nadjo, Inorg. Chem. 44 (2005) 2659–2665.
[55] B. Keita, I.M. Mbomekalle, L. Nadjo, R. Contant, Electrochem. Commun. 3 (2001) 267–273.
[56] L.H. Bi, U. Kortz, M.H. Dickman, L. Nadjo, Inorg. Chem. 44 (2005) 7485–7493.
[57] B. Keita, I.M. Mbomekalle, Y.W. Lu, L. Nadjo, P. Berthet, T.M. Anderson, C.L. Hill, Eur. J. Inorg. Chem. (2004) 3462–3475.
[58] X.Y. Zhang, M.T. Pope, M.R. Chance, G.B. Jameson, Polyhedron 14 (1995) 1381–1392.
[59] X.Y. Zhang, C.J. O'Connor, G.B. Jameson, M.T. Pope, Inorg. Chem. 35 (1996) 30–34.
[60] X.Y. Zhang, C.J. O'Connor, G.B. Jameson, M.T. Pope, Polyhedron 15 (1996) 917–922.
[61] J.F. Liu, F. Ortega, M.T. Pope, J. Chem. Soc. Dalton Trans. (1992) 1901–1906.
[62] W.L. Chen, Y.H. Wang, Y.G. Li, E.B. Wang, Y.W. Li, J. Coord. Chem. 62 (2009) 1035–1050.
[63] L.H. Bi, U. Kortz, S. Nellutla, A.C. Stowe, J. van Tol, N.S. Dalal, B. Keita, L. Nadjo, Inorg. Chem. 44 (2005) 896–903.
[64] B. Keita, E. Abdeljalil, L. Nadjo, R. Contant, R. Belghiche, Electrochem. Commun. 3 (2001) 56–62.
[65] C.C. Chen, W. Zhao, P.X. Lei, J.C. Zhao, N. Serpone, Chem. Eur. J. 10 (2004) 1956–1965.
[66] K. Lv, Y.M. Xu, J. Phys. Chem. B 110 (2006) 6204–6212.
[67] L.L. Li, Y. Chu, Y. Liu, L.H. Dong, J. Phys. Chem. C 111 (2007) 2123–2127.
[68] J.M. Gu, S.H. Li, E.B. Wang, Q.Y. Li, G.Y. Sun, R. Xu, H. Zhang, J. Solid State Chem. 182 (2009) 1265–1272.